Flux-Assisted Boron Chalcogen Mixture (BCM) Method for Synthesizing Mixed Chalcogenide Semiconductors ($AkRE_2Si_2Se_xS_{8-x}$ and $CaRE_2Si_2Se_8$) (*Ak* = Ca and Sr; *RE* = La, Ce, Pr, Nd, and Sm): Investigation of Their Magnetic and Optical Properties

Gopabandhu Panigrahi, Manish Kumar, Gregory Morrison, Christopher Sutton, and Hans-Conrad zur Loye*

Department of Chemistry and Biochemistry, University of South Carolina, Columbia, SC, 29208, United States
*E-mail: zurloye@mailbox.sc.edu

ABSTRACT:

We report a detailed structural analysis of a series of ten quaternary rare-earth-containing seleno-thiosilicates $AkRE_2Si_2Se_xS_{8-x}$ and selenosilicates, $CaRE_2Si_2Se_8$ (*Ak* = Ca and Sr; *RE* = La, Ce, Pr, Nd, and Sm). Single crystals were obtained by using the flux-assisted boron chalcogen mixture (BCM) method and single crystal X-ray diffraction was used to determine their structures. All members of the $AkRE_2Si_2Se_xS_{8-x}$ and $CaRE_2Si_2Se_8$ series crystallize in the space group $R\bar{3}c$ (space group number 167) of the trigonal crystal system. The single-crystal X-ray diffraction analysis revealed a strong preference for Se/S atoms to occupy one vs. the other of the two available sites. Polycrystalline samples were used for magnetic susceptibility and UV–visible diffuse reflectance measurements. Magnetic measurements show that $CaCe_2Si_2Se_{1.73}S_{6.27}$ and $CaNd_2Si_2Se_{2.5}S_{5.5}$ are paramagnetic with negative Weiss constants (θ = –60.1 and –26.2). Diffuse reflectance analysis gives optical band gaps of 2.7(1) eV ($CaLa_2Si_2Se_{2.38}S_{5.62}$), 2.2(1) eV ($CaCe_2Si_2Se_{1.73}S_{6.27}$), 2.5(1) eV ($CaNd_2Si_2Se_{2.5}S_{5.5}$), and 2.0(1) eV ($CaCe_2Si_2Se_8$), consistent with density functional theory calculations. By partially or fully replacing S sites with Se it was possible to achieve band gap tuning. Photoluminescence behavior was also investigated for $CaCe_2Si_2Se_{1.73}S_{6.27}$ via irradiation with 375 nm ultraviolet light.

Introduction:

A continuing challenge that solid-state chemistry deals with is to create materials with new versatile structures and compositions. Fundamentally different from organic chemistry, where a vast array of synthetic frameworks and methodologies exist for constructing complex molecules, the synthetic approaches for creating inorganic materials are noticeably fewer. Despite these limitations, there have been significant advances in the deliberate synthesis of inorganic materials.[1–4] This progress has been achieved primarily through chemical substitution, which involves replacing certain elements in a material with others, and by increasing the degree of elemental variety within the compounds.[5–7] These strategies allow researchers to tailor the properties of inorganic materials, potentially leading to the discovery of novel functionalities and applications.[8–12] Furthermore, as described herein, these synthetic approaches can in some cases be used to tune band gaps in chalcogenide semiconductors,[13,14] for example by replacing sulfur with selenium.

Rare earth-containing chalcogenides (compounds containing sulfur, selenium, or tellurium) comprise a class of materials that have been explored for use in numerous magnetic, electronic, and optical applications.[15,16] The fundamental properties of rare earth elements (REEs), when combined with chalcogenides and transition metals, often arise from the intricate electronic interactions between p, d, and f orbitals.[17–20]

The feasibility of synthesizing mixed chalcogenide compounds has attracted our interest to explore quaternary thiosilicates by partially or fully substituting sulfur (S) with selenium (Se). The successful synthesis of mixed chalcogenide compounds, where sulfur is partially or fully replaced by selenium, demonstrates the general applicability of this approach. The synthesis process invariably involves careful control of reaction conditions to ensure the desired stoichiometry and phase purity. Single-crystal XRD analysis provides detailed information on the atomic arrangement and symmetry of the synthesized compounds. This technique is crucial for identifying the exact positions and site occupancy preferences of the chalcogen anions within the crystal lattice and for understanding how selenium substitution affects the overall structure. We present a detailed structural analysis of $AkRE_2Si_2Se_xS_{8-x}$ and $CaRE_2Si_2Se_8$ (*Ak* = Ca and Sr; *RE* = La, Ce, Pr, Nd, and Sm) compounds and discuss the observed sulfur and selenium site occupancy preferences. In addition, we report on the investigation of their optical, magnetic, and photoluminescence

properties. Furthermore, the structural and electronic properties were correlated with a theoretical study *via* density functional theory (DFT) calculations.

Experimental Section:

RE_2O_3 (*RE* = La, Nd, and Sm) (99.9%, Alfa Aesar), CeO_2 (99.9%, Alfa Aesar), Pr_6O_{11} (99.9%, Alfa Aesar), sulfur powder (99.5% Fisher scientific), selenium powder (99.99% Alfa Aesar) boron (crystalline 100 mesh, 99.9%, Beantown Chemicals), SiO_2 (amorphous powder, 99.9%, Alfa Aesar), NaCl (99.9%, Alfa Aesar), $CaCl_2$ (Fisher Scientific), and $SrCl_2$ (Fisher Scientific). The $CaCl_2$-NaCl and $SrCl_2$-NaCl eutectic mixture used for synthesis was stored in a drying oven set to 260 °C to maintain the anhydrous state of the salts.

$AkRE_2Si_2Se_xS_{8-x}$ (*RE* = La, Ce, Pr, Nd and Sm; *Ak* = Ca and Sr) single crystals were synthesized by the addition of 50 mg RE_2O_3 (*RE* = La, Nd, and Sm), CeO_2, Pr_6O_{11}, 20 mg of boron, 50 mg of sulfur, 40 mg Se, and 5 mg of SiO_2 powder into a heavily carbon coated fused silica tube (12 mm outer diameter) along with 75 mg of the $CaCl_2$-NaCl eutectic mixture. The fused silica tube was evacuated to 10^{-4} torr and flame sealed using a methane/oxygen torch. The sealed fused silica tube was placed into a programmable muffle furnace set to heat to 900 °C in 20 h, dwell at this temperature for 20 h, and to cool to 750 °C in 20 h, at which point the furnace was shut off and allowed to cool down to room temperature. $SrRE_2Si_2Se_xS_{8-x}$ (*RE* =Ce and Pr) were synthesized using the same synthesis procedure except that 75 mg of the $SrCl_2$-NaCl eutectic mixture was used instead of the $CaCl_2$-NaCl mixture.

$CaRE_2Si_2Se_8$ (*RE* = La, Ce and Pr) single crystals were synthesized by the addition of 50 mg La_2O_3, CeO_2, Pr_6O_{11}, 20 mg of boron, 90 mg Se, and 5 mg of SiO_2 powder into a heavily carbon coated fused silica tube (12 mm outer diameter) along with 75 mg of the $CaCl_2$-NaCl eutectic mixture. The fused silica tube was evacuated to 10^{-4} torr and flame sealed using a methane/oxygen torch. The sealed fused silica tube was placed into a programmable muffle furnace set to heat to 850 °C in 20 h, dwell at this temperature for 20 h, and to cool to 750 °C in 20 h, at which point the furnace was shut off and allowed to cool down to room temperature.

To prepare larger quantities of samples for physical property measurements of $AkRE_2Si_2Se_xS_{8-x}$ (*Ak* = Ca and Sr) powders, the flux assisted BCM synthesis method was used, and the reactant and flux quantities were both increased two-fold. The reactants were ground using a

mortar and pestle and the ground mixture was transferred to a carbon coated fused silica tube. The reaction used the same heating profile detailed above.

The resulting product was washed three times with methanol and subjected to sonication to remove any remaining flux and other impurities. The elemental composition was analyzed by EDS analysis. The phase purity of the compounds was confirmed by powder X-ray diffraction analysis and subsequently these samples were used for physical property measurements (Figure S1-S7). The microscopic images of crystals of $AkRE_2Si_2Se_xS_{8-x}$ (*Ak* = Ca and Sr; *RE* = La, Ce, Pr, Nd, and Sm) are shown in Figure.1.

Caution: *Boron sulfides and boron selenide are prone to moisture sensitivity, leading to the generation of H_2S and H_2Se gas upon contact with water or moisture. Therefore, all reaction procedures must be conducted within fume hoods, with strict adherence to safety protocols.*

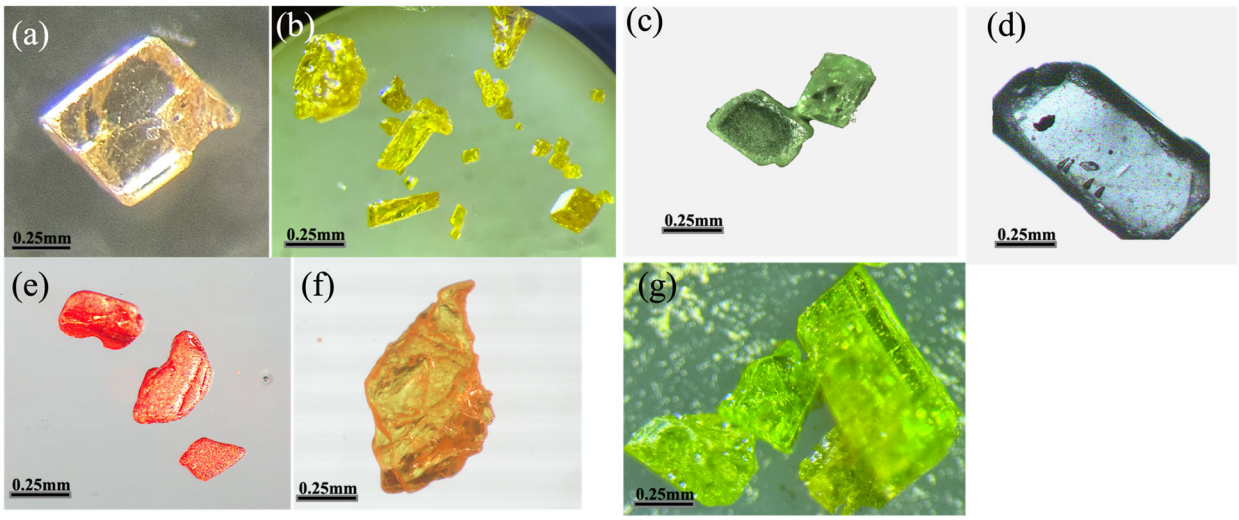

Figure.1 Optical images of (a) $CaLa_2Si_2Se_{2.38}S_{5.62}$, (b) $CaCe_2Si_2Se_{1.73}S_{6.27}$, (c) $CaPr_2Si_2Se_{1.84}S_{6.16}$, (d) $CaNd_2Si_2Se_{2.5}S_{5.5}$, (e) $CaSm_2Si_2Se_{2.47}S_{5.53}$, (f) $SrCe_2Si_2Se_{2.47}S_{5.53}$, and (g) $SrPr_2Si_2Se_{2.53}S_{5.47}$ crystals.

Single crystal X-ray Diffraction (SCXRD).

X-ray intensity data from crystals of $AkRE_2Si_2Se_xS_{8-x}$ (*Ak* = Ca and Sr; *RE* = La, Ce, Pr, Nd, and Sm) and $CaRE_2Si_2Se_8$ (*RE* = La, Ce, and Pr) were collected at 300(2) K using a Bruker D8 QUEST diffractometer equipped with a PHOTON-II area detector and an Incoatec microfocus source (Mo Kα radiation, λ = 0.71073 Å).[26] The working voltage and operating currents were 50 kV and 1.4 mA, respectively, throughout the experiment. The detector to crystal distance of 40

mm was fixed, and an exposure time of 10 sec/frame was used for the data collection. The raw area detector data frames were reduced and corrected for absorption effects using the SAINT+ and SADABS programs.[27] Final unit cell parameters were determined by least-squares refinement over large number (>9000) of reflections taken from the data set. An initial structural model was obtained with SHELXT.[28] Subsequent difference Fourier calculations and full-matrix least-squares refinement against F^2 were performed with SHELXL-2018.[29]

All $AkRE_2Si_2Se_xS_{8-x}$ (*Ak* = Ca and Sr; *RE* = La, Ce, Pr, Nd, and Sm) and $CaRE_2Si_2Se_8$ (*RE* = La, Ce, and Pr) compounds crystallize in the trigonal crystal system. The space group $R\bar{3}c$ was suggested by the pattern of systematic absences in the intensity data and was confirmed by the structure solution. The asymmetric unit of $CaRE_2Si_2Se_8$ consists of four atomic positions: one mixed *RE*/Ca site, one silicon site, and two selenium sites. In the case of $AkRE_2Si_2Se_xS_{8-x}$ compounds, each chalcogen site is modeled as a mixture of sulfur and selenium. S1/Se1 is located on a general position (site 36*f*), the *RE*/*Ak* sites are located on two-fold axes (site 18*e*), and both the Si1 and Se2/S2 sites are located on a three-fold axis (site 12*c*). Free refinement of the mixed Ak/RE sites converged to occupancies of 0.664 – 0.686 for RE and 0.313 – 0.336 for Ak. To satisfy charge neutrality the occupancies were subsequently constrained to fixed values of 2/3 RE and 1/3 Ak for all compositions. Preliminary models of $AkRE_2Si_2Se_xS_{8-x}$ (*Ak* = Ca and Sr) with the two independent chalcogen sites refined as 100% sulfur (36*f* site) and 100 % Se (12*c* site) which, however, resulted in a positive residual electron density peak located on the lighter sulfur site along with and a negative electron density centered on the heavier selenium site. Trial refinements of the site occupation factor for both sites showed an increase from 100% sulfur or a decrease from 100% Se. Residual electron density peaks corresponding to discrete S and Se positions did not appear in the difference maps and therefore separate S and Se sites could not be resolved. This is likely because of the close similarity of Si-S and Si-Se distances, with the slight positional deviations accounted for by the anisotropic displacement parameters. Two mixed S1/Se1 and Se2/S2 positions were refined, with identical coordinates for S and Se at each site, with the occupancies of each site constrained to sum to one. All atoms were refined with anisotropic displacement parameters. The largest residual electron density peak and hole in the final difference map, site occupancy, summary of the crystallographic and refinement data for all title compounds is provided in Table 1 and Table S1.

Table 1. Crystallographic information of *Ak*$RE_2Si_2Se_xS_{8-x}$ *and* Ca$RE_2Si_2Se_8$ (*Ak* = Ca and Sr; *RE* = La, Ce, Pr, Nd, and Sm)

Chemical formula	**$CaLa_2Si_2Se_{2.38}S_{5.62}$**	**$CaCe_2Si_2Se_{1.73}S_{6.27}$**	**$CaPr_2Si_2Se_{1.84}S_{6.16}$**	**$CaNd_2Si_2Se_{2.5}S_{5.5}$**	**$CaSm_2Si_2Se_{2.47}S_{5.53}$**
Color	White	Yellow	Green	Blue	Yellow
Formula weight	742.09	714.20	720.93	758.30	769.44
space group			$R\bar{3}c$		
Temperature (K)	299(2)	298(2)	300(2)	300(2)	300(2)
***a* (Å)**	9.1791(3),	9.0934(1),	9.0643(2),	9.0638(2),	9.0164(2),
***c* (Å)**	26.6474(11)	26.4334(4)	26.3441(7)	26.3114(7)	26.1646 (6)
V (Å^3)	1944.40(15)	1892.94(7)	1874.49(6)	1871.95(10)	1842.09 (10)
Density (mg/m^3)	3.802	3.759	3.832	4.025	4.162
abs coeff (mm^{-1})	14.611	13.70	14.65	16.88	18.30
Z	6.0	6.0	6.0	6.0	6.0
R_{int}	0.037	0.028	0.025	0.032	0.028
***R*1, *wR*2**	0.017, 0.037	0.015, 0.033	0.017, 0.037	0.016, 0.037	0.019, 0.042
GOF (F^2)	1.13	1.13	1.12	1.13	1.13
$\Delta\rho_{max}$, $\Delta\rho_{min}$ (eÅ^{-3})	1.17, -0.91	1.05, -0.83	1.24, -1.0	1.29, -1.13	1.68, -1.43
Chemical formula	**$SrCe_2Si_2Se_{2.47}S_{5.53}$**	**$SrPr_2Si_2Se_{2.53}S_{5.47}$**	**$CaLa_2Si_2Se_8$**	**$CaCe_2Si_2Se_8$**	**$CaPr_2Si_2Se_8$**
Color	Yellow	Green	Yellow	Yellow	Green
Formula weight	796.21	800.58	1005.74	1008.16	1009.74
space group			*R*-3*c*		
Temperature (K)	299(2)	299(2)	299(2)	298(2)	299(2)
***a* (Å)**	9.1694(1)	9.1413(3)	9.3837(2)	9.3391(2)	9.3095(2)
***c* (Å)**	26.7907(3)	26.6847(8)	27.8182(8)	27.6469(8)	27.5108(6)
V (Å^3)	1950.73(8)	1931.12(7)	2120.92(10)	2088.27(10)	2064.84(10)
Density (mg/m^3)	4.067	4.131	4.725	4.810	4.872
abs coeff (mm^{-1})	18.90	19.75	27.04	27.87	28.65
Z	6.0	6.0	6.0	6.0	6.0
R_{int}	0.026	0.034	0.033	0.031	0.032
***R*1, *wR*2**	0.023, 0.064	0.026, 0.059	0.025, 0.051	0.026, 0.053	0.033, 0.096
GOF (F^2)	1.18	1.11	1.11	1.09	1.27
$\Delta\rho_{max}$, $\Delta\rho_{min}$ (eÅ^{-3})	2.40, -1.87	2.33, -2.68	2.00, -2.08	1.66, -2.17	2.10, -1.83

Powder X-ray Diffraction (PXRD).

Powder X-ray diffraction (PXRD) data were obtained by analyzing finely ground powder samples of $AkRE_2Si_2Se_xS_{8-x}$ prepared using the flux assisted BCM synthesis method. PXRD data were collected on a Bruker D2 PHASER diffractometer using Cu-Kα radiation (λ = 1.5418 Å) over the 2θ range 5-65 ° with a step size of 0.02°.

Energy-Dispersive X-Ray Spectroscopy (EDS).

EDS data were collected on single crystals by mounting them directly onto a SEM stub using conducting carbon tape. Quantitative elemental analysis was performed utilizing a Tescan Vega-3 SEM instrument, which was fitted with a Thermo EDS attachment. The SEM operated in a low-vacuum mode with a 15-20 kV accelerating voltage and a 60-second accumulation time. The summarized SEM results can be found in the supporting information (Table S3).

UV-Visible Spectroscopy.

UV-visible reflectance spectra were recorded using a Perkin-Elmer lambda 35 UV-vis spectrophotometer. The spectrophotometer was operated in the diffuse reflectance mode and was equipped with an integrating sphere. Reflectance data were converted internally to absorbance via the Kubelka-Munk function. Spectra were recorded over the 250 nm – 900 nm range at room temperature and ambient condition on powder samples.

Photoluminescence.

Micro-photoluminescence (μ-PL) measurements were performed using a single crystal of $CaCe_2Si_2Se_{1.73}S_{6.27}$ to investigate the optical emission properties of the synthesized materials. The data were collected using a HORIBA Scientific microscope-based spectroscopy system, which integrates a high-resolution HORIBA iHR320 imaging spectrograph and a Synapse CCD detector for precise spectral analysis. Excitation was provided by a confocal 375 nm diode laser, chosen for its stability and suitability for UV-range excitation. The excitation beam was focused onto the crystal surface through a 10× UV objective lens, allowing for spatially resolved photoluminescence measurements at the microscale. The emission spectra were recorded in the range of 400 to 800 nm using LabSpec 6 software, under a constant laser power of 10.0 mW.

Theoretical Calculation:

The spin-polarized DFT calculations were performed using the Vienna *ab initio* simulation package (VASP).[30,31] The ion-electron interactions were taken into account by projector-augmented wave (PAW) pseudopotentials[32] of each species. Specifically, the PAW pseudopotentials Ca (Ca_sv), Ce (Ce_3), Si (Si), Se (Se), and S (S) were considered for calculations. The structures were relaxed, and the density of states was calculated using the PBE[33] exchange-correlation functional. The self-consistency loop was converged with a total energy threshold of 10^{-6} eV. The geometries were optimized until the Hellmann-Feynman forces acting on atoms were smaller than 0.01 eV/Å. The planewave kinetic energy cutoff of 520 eV was used for basis set expansion. A Γ-centered 3×3×1 *k*-mesh was used for Brillouin zone sampling. We used a 78-atom cell, containing six formula units. For mixing of the sites, we used the Ewald approach as implemented in Pymatgen.[34] For $CaCe_2Si_2Se_8$, we considered the top five cation (Ca/Ce) orderings and used the lowest-energy ordering obtained from DFT. Further, we fixed the cation sites and obtained the lowest-energy structure from the top five anion (S/Se) orderings in $CaCe_2Si_2Se_2S_6$. We found that these structures for $CaCe_2Si_2Se_8$ and $CaCe_2Si_2Se_2S_6$ were more stable than the special quasirandom structures (SQS)[35,36] by 12.47 and 34.33 meV/atom, respectively. In low-energy ordering of $CaCe_2Si_2Se_2S_6$, Se is preferred at the Q1 site as described in the crystal structure subsection.

Result and discussion

Synthesis: Building on our previous research on the $AkRE_2Si_2S_8$ series, we have extended the synthesis to $CaRE_2Si_2Se_8$ and $AkRE_2Si_2Se_xS_{8-x}$ (Ak = Ca and Sr; *RE* = La, Ce, Pr, Nd, and Sm) compounds using the flux-assisted BCM method, incorporating modifications into the heating profiles and elemental compositions.[1,13,37–39] The RE_2O_3 and SiO_2 oxide reagents served as the rare earth and silicon sources, and boron was used to remove the oxygen from the oxide reagents, thus leaving these elements available for reacting with the elemental sulfur and selenium to form the chalcogenides.[1,40] In this synthesis, the eutectic mixtures of $CaCl_2$/NaCl and $SrCl_2$/NaCl functioned both as a flux and as the source of calcium and strontium. This approach enabled us to synthesize ten new compounds within the $CaRE_2Si_2Se_8$ and $AkRE_2Si_2Se_xS_{8-x}$ series (*RE* = La, Ce, Pr, Nd, and Sm) by varying the lanthanide RE_2O_3 reagent from *RE* = La to Sm. EDS analyses revealed the presence of the predicted elements in the crystals (Table S3) and confirmed the absence of any extraneous elements. We also performed EDS mapping on crystals of $CaPr_2Si_2Se_{1.84}S_{6.16}$, and $CaNd_2Si_2Se_{2.47}S_{5.53}$ to visualize the elemental distribution, which indicates a uniform distribution of all elements throughout the crystals (Figure 2).

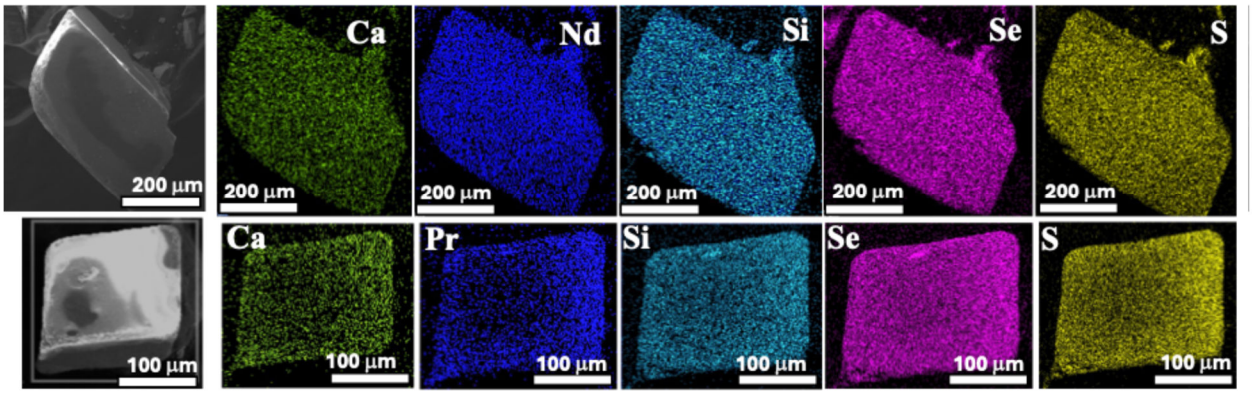

Figure.2 SEM image and elemental mapping of (a) $CaPr_2Si_2Se_{1.84}S_{6.16}$, and (b) $CaNd_2Si_2Se_{2.47}S_{5.53}$ crystals.

Despite our efforts to incorporate the smaller lanthanides, we were unable to obtain compositions containing rare earth elements smaller than samarium with mixed sulfide / selenide compositions. To target additional compositions, we explored the substitution of Sr for Ca, which enabled us to synthesize two new Sr-based quaternary thioselenosilicates, $SrRE_2Si_2Se_xS_{8-x}$ (RE = Ce, Pr). The Sr for Ca substitution was accomplished by changing the flux from $CaCl_2$/NaCl to

$SrCl_2$/NaCl. In addition to the mixed chalcogenide compounds, we successfully synthesized three quaternary selenides, $CaRE_2Si_2Se_8$ (RE = La, Ce, and Pr). However, the yield of crystalline products in this selenide series was significantly lower compared to their sulfide and mixed sulfide-selenide analogues. While phase-pure polycrystalline samples were obtained for all Ca- and Sr-based mixed chalcogenides, only $CaCe_2Si_2Se_8$ could be isolated as a phase-pure polycrystalline material within the $CaRE_2Si_2Se_8$ series. All attempts to synthesize Sr-based selenide analogues were unsuccessful, and no crystalline or phase-pure $SrRE_2Si_2Se_8$ compounds could be obtained under the explored reaction conditions.

The products of the $CaCe_2Si_2Se_8$ and $AkRE_2Si_2Se_xS_{8-x}$ reactions were washed with methanol to dissolve the flux and to remove impurities, resulting in phase-pure samples (see Figure S1-S7 for PXRD patterns). This also allowed us to determine that these phases are stable to ambient conditions. The experimental and calculated PXRD patterns of $CaCe_2Si_2Se_{1.73}S_{6.27}$ and $CaCe_2SiSe_8$, as shown in Figure 3, exhibit a noticeable shift of the diffraction peaks toward lower angles (larger lattice parameters) when compared to our previously reported compound $CaCe_2Si_2S_8$. This systematic leftward shift in the peak positions is a clear indication of the progressive substitution of sulfur (S) atoms by the larger selenium (Se) atoms in the crystal lattice. As the selenium content increases, the unit cell expands due to the larger ionic radius of Se^{2-} compared to S^{2-}, leading to a more pronounced shift in the diffraction peaks.

Crystal Structure: The compounds $CaCe_2Si_2Se_8$ and $AkRE_2Si_2Se_xS_{8-x}$**,** synthesized via the flux-assisted BCM method, crystallize in the $R\bar{3}c$ space group. This structure is isostructural with the previously reported $Eu_3As_2S_8$, lead-based series $RE_2PbSi_2S_8$ (RE = Y, Ce, Pr, Nd, Sm, Gd, Tb, Dy, Ho) and $BaLa_2Si_2S_8$.[416,42]

In the mixed chalcogenide compounds$AkRE_2Si_2Se_xS_{8-x}$ (where Ak = Ca and Sr and RE = La, Ce, Pr, Nd, and Sm), the selenium (Se) and sulfur (S) atoms are distributed preferentially within the crystal lattice governed by their local bonding environments. The crystal structure contains two nonequivalent chalcogen positions, referred to as Q1 and Q2 (Q = S + Se). These sites differ in their coordination geometry and bonding characteristics with surrounding metal atoms. It has been observed that the Q1 site preferentially incorporates sulfur, while the Q2 site is more favorable for selenium substitution. This selective distribution arises from intrinsic differences in the atomic size and electronegativity of S and Se. The thiosilicate group contains four S/Se sites, three Q1 and one Q2, where the Si-Q1 bond is slightly shorter than the Si-Q2 bond. Sulfur, being smaller (atomic

radius ≈ 1.84 Å) and more electronegative (2.58 on the Pauling scale), tends to occupy the Q1 sites where the bonding environment is more compact and ionic. In these sites, sulfur forms stronger and shorter metal–sulfur bonds, leading to a more stable local structure. In contrast, selenium, which has a larger atomic radius (≈ 1.98 Å) and slightly lower electronegativity (2.55), preferentially occupies the Q2 sites that offer a more open and covalent bonding environment. Here, Se can form weaker and longer metal–selenium bonds, which better accommodate its larger size and more polarizable nature.

The unit cell contains four independent atomic sites, with the metal site 18*e* being occupied by both rare earth and alkaline earth cations. For each composition, the occupancy factor of the 18*e* metal site was refined, resulting in a numerical value close to 2/3 *RE* + 1/3 *Ak*, aligning well with the expected ratio based on charge balance. Consequently, the mixed metal site occupancies were fixed as 2/3 *RE* + 1/3 *Ak* in all $CaCe_2Si_2Se_8$ and $AkRE_2Si_2Se_xS_{8-x}$ compounds throughout the final refinement process. The crystal data and refinement details are summarized in Table 1 and Table S1.

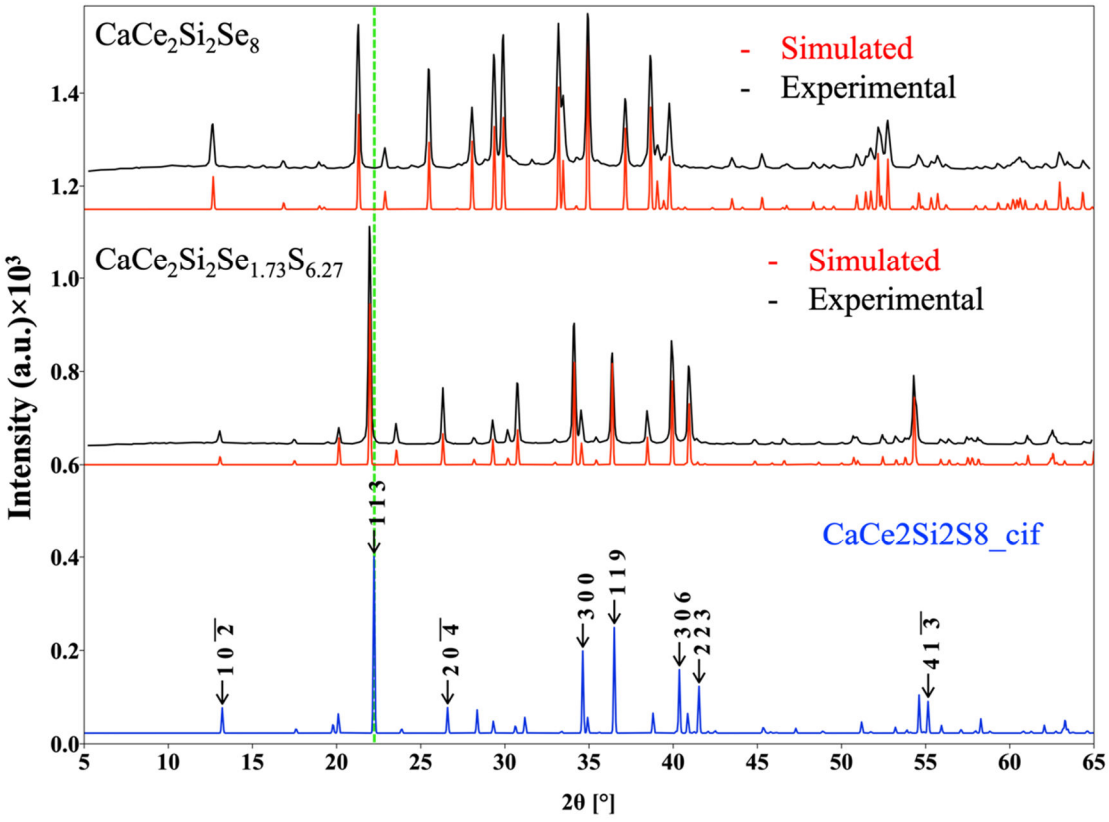

Figure.3 The PXRD pattern of polycrystalline $CaCe_2Si_2Se_{1.73}S_{6.27}$ and $CaCe_2SiSe_8$ samples with the peak shifts referenced to $CaCe_2SiS_8$.

The unit cell structure of $CaCe_2Si_2Se_8$ and $AkRE_2Si_2Se_xS_{8-x}$ along the *c*-direction is shown in Figure 4b, illustrating how the 3-D structure is formed by edge- and corner-sharing of neighboring $(1/3RE+1/3Ak)Q_8$ bi-capped trigonal prisms and $SiSQ(1)Q(2)_3$ tetrahedral units. Figure 4a depicts the repeating unit of the structure, which consists of six $(1/3RE+1/3Ak)Q_8$ and one $SiQ(1)Q(2)_3$ units. The edge- and corner-sharing $(1/3RE+1/3Ak)S_8$ bi-capped trigonal prisms create tetrahedral cavities in which the silicon cations are located.

The RE–Q (Q = S + Se) bond lengths in the bi-capped trigonal prisms vary depending on the rare earth element and chalcogen composition. In the mixed chalcogenide series, $CaRE_2Si_2Se_xS_{8-x}$, these bond lengths range from 3.2724(5) Å to 2.7855(6) Å for La to Sm, while in the same series, the corresponding Si–Q bond lengths within the irregularly shaped SiQ_4 tetrahedra range from 2.1341(6) Å to 2.2568(12) Å. Similarly, the RE–Q bond distances in $SrRE_2Si_2Se_xS_{8-x}$ compositions extend from 3.2729(11) Å to 2.8468(10) Å, while the Si–Q bonds range from 2.2588(11) Å to 2.1558(18) Å. These values align well with previously reported chalcogenide structures, suggesting a consistent structural motif across these materials.[43,43–48]

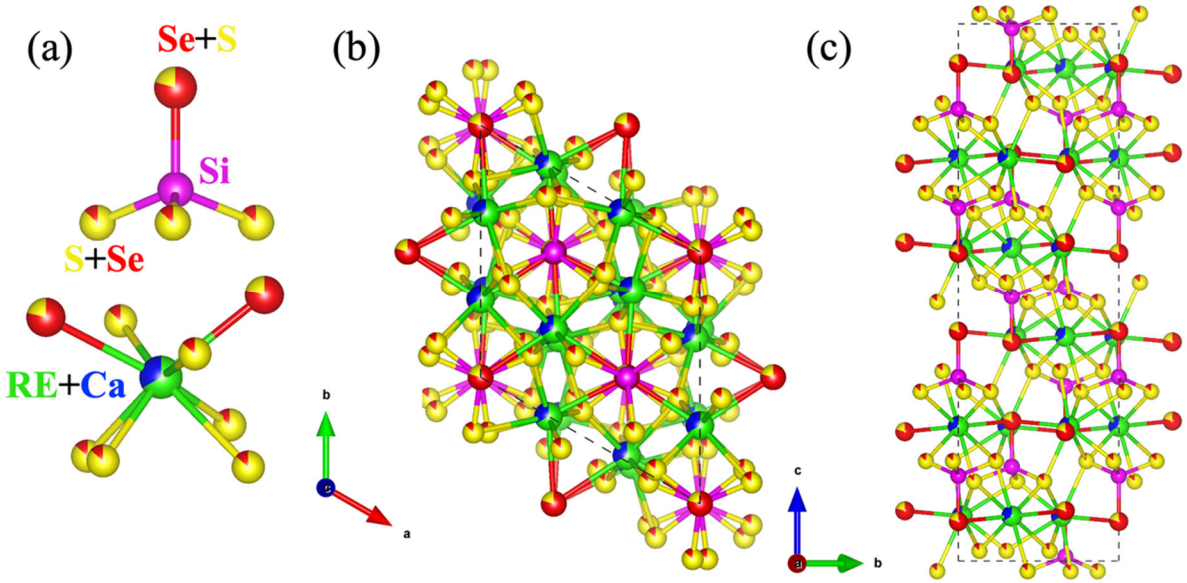

Figure 4. The (a) repeating unit (SiQ_4 and $Ak+REQ_8$), (b) unit cell representation of $AkRE_2Si_2S_{8-x}Se_x$ along *c*-direction and (c) *b*-direction.

In the $CaRE_2Si_2Se_8$ series, the RE–Se bond lengths are generally larger due to the increased atomic radius of selenium compared to sulfur. Specifically, in the bi-capped trigonal prisms, the RE–Se bond lengths range from 3.4019(6) Å to 2.9203(8) Å for La to Pr in the selenide-rich compositions. The again irregularly shaped $SiSe_4$ tetrahedra in these structures exhibit Si–Se bond lengths ranging from 2.604(10) Å to 2.2756(12) Å.

Magnetic properties: The temperature dependence of the magnetic susceptibility was measured over the temperature range of 2K - 300 K using phase pure polycrystalline samples of $CaCe_2Si_2Se_{1.73}S_{6.27}$ and $CaNd_2Si_2Se_{2.47}S_{5.53}$. The temperature dependence of the magnetic susceptibility (χ) follows the Curie law down to 2 K; no evidence of long-range magnetic ordering was observed. The χ *vs.* T plots for $CaCe_2Si_2Se_{1.73}S_{6.27}$ and $CaNd_2Si_2Se_{2.47}S_{5.53}$ are shown in Figures 5a and 5c. The high temperature region (200-300 K) of the inverse susceptibility data were used for the Curie law fit the to calculate the Curie (C) and Weiss (θ) constants.

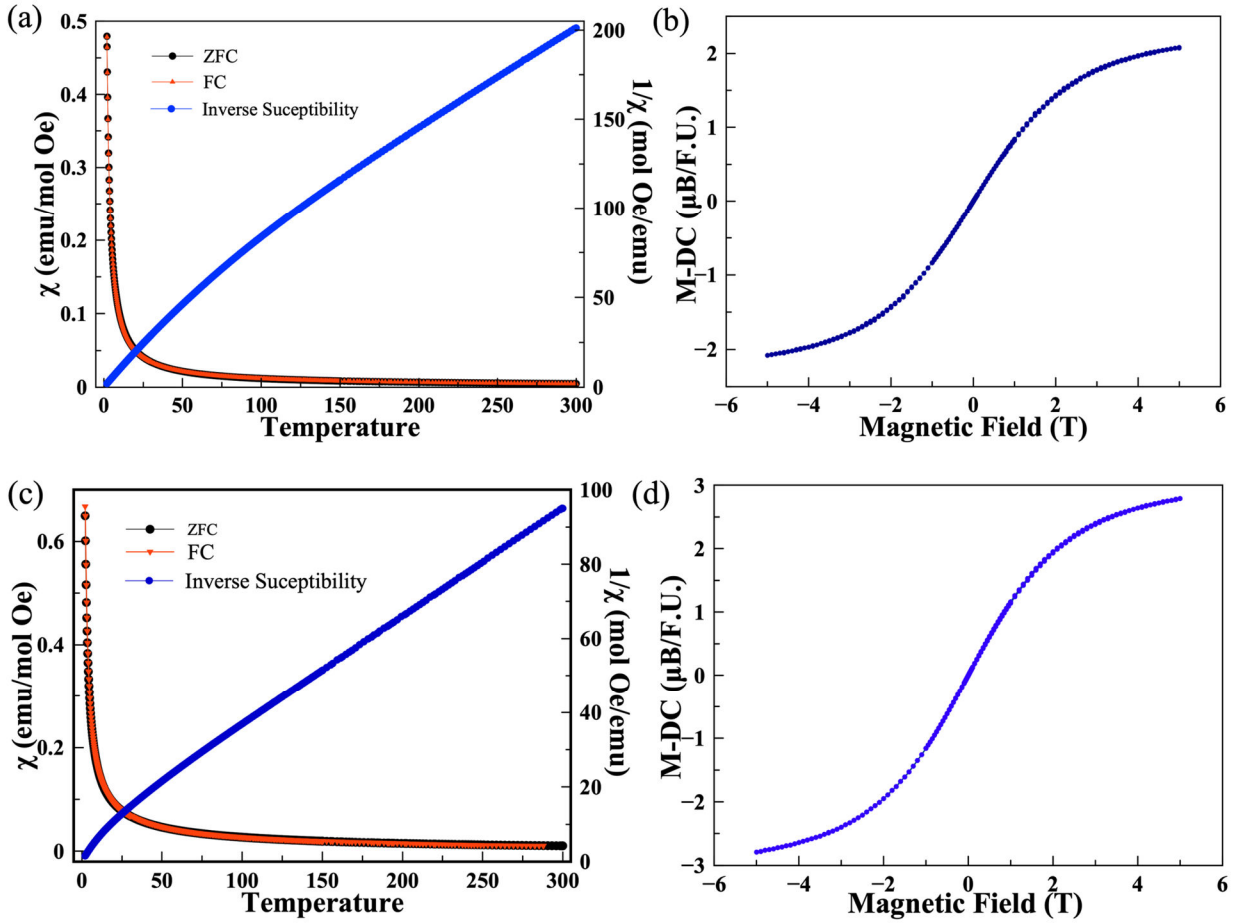

Figure 5. Magnetic susceptibility and inverse susceptibility vs temperature plots for (a) $CaCe_2Si_2Se_{1.73}S_{6.27}$ and (c) $CaNd_2Si_2Se_{2.47}S_{5.53}$ and (b) and (d) magnetization vs. applied field plots for $CaCe_2Si_2Se_{1.73}S_{6.27}$ and $CaNd_2Si_2Se_{2.47}S_{5.53}$ measured at 2 K.

The effective magnetic moments are 3.78 μ_B and 5.11 μ_B per formula unit for the Ce and Nd composition, respectively, in good agreement with those expected for Ce^{3+} and Nd^{3+} ions, 3.54μ_B and 5.12μ_B respectively. The negative Weiss constants (-60.1 and -26.2) observed for $CaCe_2Si_2Se_{1.73}S_{6.27}$ and $CaNd_2Si_2Se_{2.47}S_{5.53}$ compounds is likely due to crystal electric field effects. No differences between the field-cooled (FC) and zero field-cooled (ZFC) data for either composition were observed; the FC data and ZFC data are shown in Figure 5a and 5c. The 2K M *vs.* H plot data for the two samples, reveal the saturation of the magnetic moments at the highest magnetic fields (Figures 5b and 5d).

UV-Visible Diffuse Reflectance Spectroscopy:

The optical properties of the quaternary compounds $CaLa_2Si_2Se_{2.38}S_{5.62}$, $CaCe_2Si_2Se_{1.73}S_{6.27}$, $CaNd_2Si_2Se_{2.5}S_{5.5}$, and the quaternary compound $CaCe_2Si_2Se_8$ were examined using polycrystalline powders. As expected, many weak absorption peaks were observed due to the f-f electronic transitions of the RE^{3+} cations. The Kubelka-Munk equation was employed to analyze the optical absorption data, as shown in Figures 6(a-d). The absorption plots are consistent with band gaps of 2.7(1) eV ($CaLa_2Si_2Se_{2.38}S_{5.62}$), 2.2(1) eV ($CaCe_2Si_2Se_{1.73}S_{6.27}$, 2.5(1) eV ($CaNd_2Si_2Se_{2.5}S_{5.5}$) and 2.0(1) eV ($CaCe_2Si_2Se_8$), indicating the semiconducting nature of the studied thiosilicates. The reduction of the band gap energy observed for the selenothio-silicate and seleno-silicates, as compared to our previously reported thiosilicates ($CaCe_2Si_2S_8$, 2.5(1) eV), is presumably due to the replacement of S with Se in the quaternary compounds.

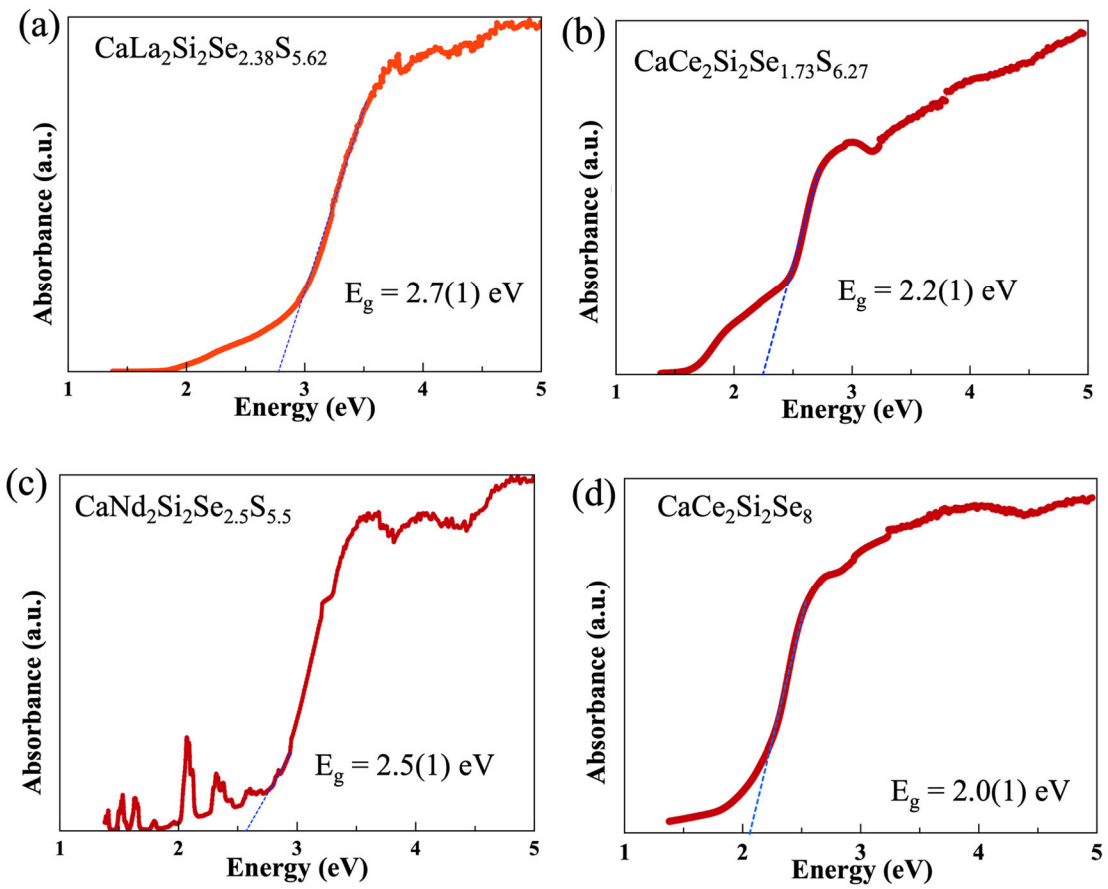

Figure 6. The optical absorption plot of polycrystalline samples **(a)** $CaLa_2Si_2Se_{2.38}S_{5.62}$, (b) $CaCe_2Si_2Se_{1.73}S_{6.27}$, (c) $CaNd_2Si_2Se_{2.5}S_{5.5}$, and **(d)** $CaCe_2Si_2Se_8$.

Atom-projected partial density of states (pDOS), calculated using DFT for $CaCe_2Si_2Se_2S_6$ and $CaCe_2Si_2Se_8$, show band gaps of 2.51 and 2.01 eV, respectively (see Figure 7), corroborating the experimentally calculated band gaps. Moreover, we have also plotted the band structure for $CaCe_2Si_2Se_2S_6$ and $CaCe_2Si_2Se_8$ which indicate that both materials exhibit an indirect band gap with an energy of 2.51 eV and 2.01 eV, respectively, whereas the direct band gaps of these materials are slightly higher (by ~ 0.07 eV) with an energy of 2.58 eV and 2.08 eV. The valence band maximum (VBM) is mainly composed of S/Se-orbitals, while Ce-orbitals contribute to the conduction band minimum (CBm). Orbitals of Si and Ca mainly appear deep inside the valence and conduction bands, respectively. The smaller band gap in the case of $CaCe_2Si_2Se_8$ is attributed to the Se *p*-orbitals, which lifts the VBM.

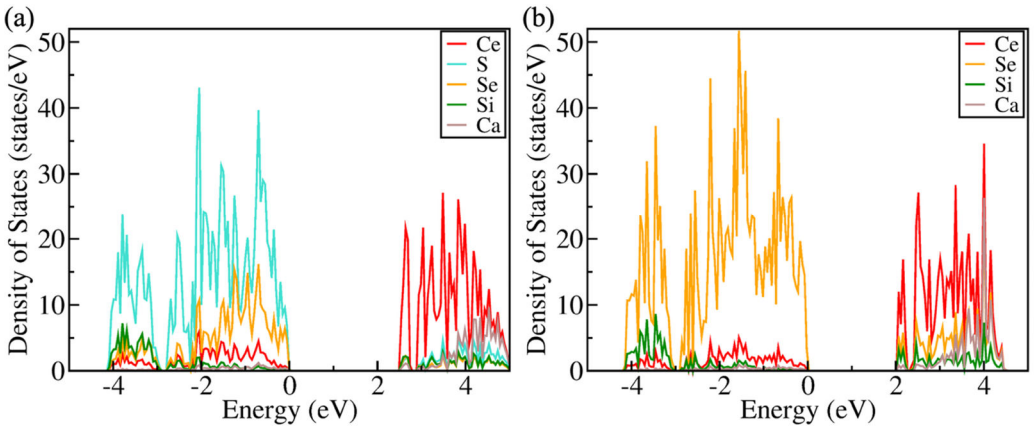

Figure 7. Atom-projected partial density of states for **(a)** $CaCe_2Si_2Se_2S_6$ and **(b)** $CaCe_2Si_2Se_8$. The Fermi level is set at 0 eV.

Photoluminescence.

Photoluminescence (PL) spectra were collected using single crystals of $CaCe_2Si_2Se_{1.73}S_{6.27}$ to investigate the optical emission properties. The measurements were made using a 375 nm excitation source. Upon excitation, the $CaCe_2Si_2Se_{1.73}S_{6.27}$ crystals exhibit strong green luminescence, although the emission intensity was noticeably lower than that of the previously reported $CaCe_2Si_2S_8$ compound. The PL spectrum of $CaCe_2Si_2Se_{1.73}S_{6.27}$ displayed a broad emission band located at ~525 nm that is due to the characteristic 5d–4f electronic transition of the Ce^{3+} ion (Figure 8a).

Notably, the emission peak of the mixed-anion compound appeared broader in comparison to its sulfur-only analogue. This enhanced peak broadening is likely a result of inhomogeneous broadening effects arising from the substitutional doping in the mixed chalcogenide system. The presence of both selenium and sulfur in the lattice introduces local variations in the crystal field environment and bonding, which can lead to the formation of localized electronic states with slightly different energies. Incorporation of Se leads to increased structural distortion and apparently lead to more non-radiative pathways that effectively quench the luminescence. Such compositional disorder contributes to the observed spectral broadening and may also influence the overall luminescence efficiency. The composition $CaCe_2Si_2Se_8$ did not exhibit luminescence under UV light and no further optical studies were performed using this compound. The yellow polycrystalline powder sample of $CaCe_2Si_2Se_{1.73}S_{6.27}$ looks green under UV light, as shown in Figure 8b.

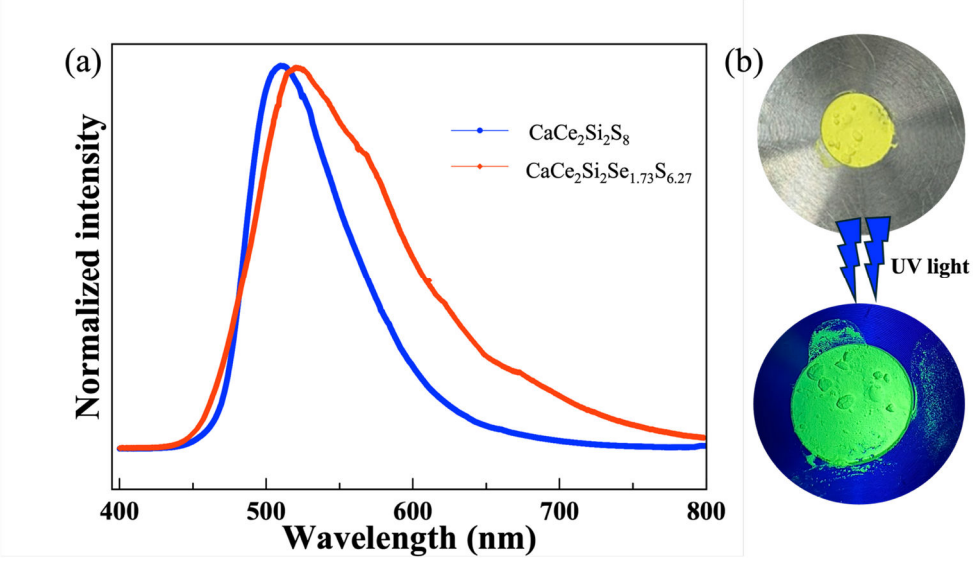

Figure 8. Emission spectra of (a) $CaCe_2Si_2Se_{1.73}S_{6.27}$ compare with $CaCe_2Si_2S_8$ crystals at room temperature under 375 nm excitation and (b) Green luminescence of $CaCe_2Si_2Se_{1.73}S_{6.27}$ under UV light

Conclusion:

The ability to synthesize mixed chalcogenide compounds has significantly advanced the study of quaternary thiosilicates, particularly in the $AkRE_2Si_2Se_xS_{8-x}$ (Ak = Ca, Sr; RE = La, Ce, Pr, Nd, Sm) and $CaCe_2Si_2Se_8$ systems. These advancements have been primarily driven by elemental substitutions, which play a crucial role in tailoring the structural and physical properties of these materials. Specifically, the substitution of Sr with Ca or the replacement of sulfur with selenium leads to the formation of new compositions with distinct characteristics. Structural characterization using single-crystal X-ray diffraction (XRD) analysis has provided a comprehensive understanding of their crystal chemistry. Additionally, investigations into their physical properties, including magnetic behavior and optical band gaps, have yielded valuable insights. Notably, the substitution of sulfur by selenium induces a gradual reduction in the optical band gap, transitioning from higher to lower values. Magnetic studies revealed a negative Weiss constant of -26.2 K for $CaNd_2Si_2Se_{2.47}S_{5.53}$, which is indicative of the presence of antiferromagnetic correlations. These findings can open avenues for further exploration into magnetic properties through additional compositional modifications.

Notes

The authors declare no competing financial interest.

Associated Content

Supporting Information

The supporting information: EDS results, PXRD patterns, crystallographic tables; tables of bond lengths; band structure diagrams (PDF). This information is available free of charge at the website XXX

The CCDC 2424988-2424997 entries encompass the supplementary crystallographic data associated with this paper. These data are accessible without charge through www.ccdc.cam.ac.uk/data_request/cif, or by sending a request via email to data_request@ccdc.cam.ac.uk, or by directly contacting The Cambridge Crystallographic Data Centre at 12 Union Road, Cambridge CB2 1EZ, UK; fax: +44 1223 336033. The supporting information (SI) file contains EDS results, TGA plots, and PXRD patterns of title compounds.

ACKNOWLEDGMENTS

The authors gratefully acknowledge the support from the U.S. Department of Energy, Office of Basic Energy Sciences, Division of Materials Sciences and Engineering, under award DE-SC0018739. Synthesis, structural characterization, optical, Photoluminescence, magnetic studies and theoretical calculations were conducted at the University of South Carolina.

References:

(1) Breton, L. S.; Klepov, V. V.; zur Loye, H.-C. Facile Oxide to Chalcogenide Conversion for Actinides Using the Boron–Chalcogen Mixture Method. *J. Am. Chem. Soc.* **2020**, *142* (33), 14365–14373.

(2) Bugaris, D. E.; zur Loye, H.-C. Materials Discovery by Flux Crystal Growth: Quaternary and Higher Order Oxides. *Angew. Chem. Int. Ed.* **2012**, *51* (16), 3780–3811.

(3) Phelan, W. A.; Menard, M. C.; Kangas, M. J.; McCandless, G. T.; Drake, B. L.; Chan, J. Y. Adventures in Crystal Growth: Synthesis and Characterization of Single Crystals of Complex Intermetallic Compounds. *Chem. Mater.* **2012**, *24* (3), 409–420.

(4) Kravchuk, D. V.; Wilson, R. E. Stoichiometric Lanthanide Compounds with Diglycolamides: A Synthetic Approach toward Understanding Rare-Earth Speciation in Solution. *Inorg. Chem.* **2024**, *63* (46), 22049–22060.

(5) Tassanov, A.; Lee, H.; Xia, Y.; Hodges, J. M. Layered $NaBa_2M_3Q_3(Q_2)$(M= Cu or Ag; Q = S or Se) Chalcogenides and Local Ordering in Their Mixed-Anion Compositions. *Inorg. Chem.* **2024**, *63* (34), 15584–15591.

(6) Daszkiewicz, M.; Marchuk, O. V.; Gulay, L. D.; Kaczorowski, D. Crystal Structures and Magnetic Properties of $R_2PbSi_2S_8$ (R = Y, Ce, Pr, Nd, Sm, Gd, Tb, Dy, Ho), $R_2PbSi_2Se_8$ (R = La, Ce, Pr, Nd, Sm, Gd) and $R_2PbGe_2S_8$ (R = Ce, Pr) Compounds. *J. Alloys Compd.* **2012**, *519*, 85–91.

(7) Mumbaraddi, D.; Mishra, V.; Jomaa, M.; Liu, X.; Karmakar, A.; Thirupurasanthiran, S.; Michaelis, V. K.; Grosvenor, A. P.; Meldrum, A.; Mar, A. Controlling the Luminescence of Rare-Earth Chalcogenide Iodides $RE_3(Ge_{1-x}Si_x)_2S_8I$ (RE = La, Ce, and Pr) and $Ce_3Si_2(S_{1-y}Se_y)_8I$. *Chem. Mater.* **2023**, *35* (15), 6039–6049.

(8)Benck, J. D.; Hellstern, T. R.; Kibsgaard, J.; Chakthranont, P.; Jaramillo, T. F. Catalyzing the Hydrogen Evolution Reaction (HER) with Molybdenum Sulfide Nanomaterials. *Acs Catal.* **2014**, *4* (11), 3957–3971.

(9)Lee, M. M.; Teuscher, J.; Miyasaka, T.; Murakami, T. N.; Snaith, H. J. Efficient Hybrid Solar Cells Based on Meso-Superstructured Organometal Halide Perovskites. *science* **2012**, *338* (6107), 643–647.

(10)Kanatzidis, M. G. Discovery-Synthesis, Design, and Prediction of Chalcogenide Phases. *Inorg. Chem.* **2017**, *56* (6), 3158–3173.

(11)Goodenough, J. B.; Park, K.-S. The Li-Ion Rechargeable Battery: A Perspective. *J. Am. Chem. Soc.* **2013**, *135* (4), 1167–1176.

(12)Panigrahi, G.; Yadav, S.; Jana, S.; V. Ramanujachary, K.; K. Niranjan, M.; Prakash, J. Ba_4FeAgS_6: A New Antiferromagnetic and Semiconducting Quaternary Sulfide. *Dalton Trans.* **2023**, *52* (3), 621–634.

(13)Panigrahi, G.; Morrison, G.; Smith, M. D.; zur Loye, H.-C. Synthesis, Optical, and Magnetic Properties of the Mixed Chalcogenide Semiconductor Series $Eu(II)_2SiSe_xS_{4-x}$, Prepared via the Flux-Assisted Boron Chalcogen Mixture Method. *Inorg. Chem.* **2024**, *63* (50), 23802–23809.

(14)Dey, T.; Mumbaraddi, D.; Wen, F.; Mishra, V.; Michaelis, V. K.; Mar, A. Are Selenides the Same as Sulfides? Structure, Spectroscopy, and Properties of Narrow-Gap Rare-Earth Semiconductors $RE_2Sn(S_{1-x}Se_x)_5$ (*RE* = La, Ce; x = 0–0.8). *Inorg. Chem.* **2024**, *63* (23), 10726–10736.

(15)Panigrahi, G.; Jana, S.; Ishtiyak, M.; Tripathy, B.; Malladi, S. K.; Niranjan, M. K.; Prakash, J. Chalcogen Dependent Metal Vacancies and Disorder in $Ba_2Ln_{1-x}Mn_{2-y}S_5$ and $Ba_{2-\delta}Ln_{1-x}Mn_{2-y}Se_5$ (*Ln* = Pr, Nd, and Gd) Structures. *J. Alloys Compd.* **2022**, *901*, 163607.

(16)Mitchell, K.; Huang, F. Q.; Caspi, E. N.; McFarland, A. D.; Haynes, C. L.; Somers, R. C.; Jorgensen, J. D.; Van Duyne, R. P.; Ibers, J. A. Syntheses, Structure, and Selected Physical Properties of $CsLnMnSe_3$ (Ln= Sm, Gd, Tb, Dy, Ho, Er, Tm, Yb, Y) and $AYbZnQ_3$ (A= Rb, Cs; Q = S, Se, Te). *Inorg. Chem.* **2004**, *43* (3), 1082–1089.

(17)Woods-Robinson, R.; Han, Y.; Zhang, H.; Ablekim, T.; Khan, I.; Persson, K. A.; Zakutayev, A. Wide Band Gap Chalcogenide Semiconductors. *Chem. Rev.* **2020**, *120* (9), 4007–4055.

(18) Vajenine, G. V.; Hoffmann, R. Compounds Containing Copper− Sulfur Layers: Electronic Structure, Conductivity, and Stability. *Inorg. Chem.* **1996**, *35* (2), 451–457.

(19) Mitchell, K.; Huang, F. Q.; McFarland, A. D.; Haynes, C. L.; Somers, R. C.; Van Duyne, R. P.; Ibers, J. A. The $CsLnMSe_3$ Semiconductors (Ln= Rare-Earth Element, Y; M= Zn, Cd, Hg). *Inorg. Chem.* **2003**, *42* (13), 4109–4116.

(20) Mitchell, K.; Ibers, J. A. Rare-Earth Transition-Metal Chalcogenides. *Chem. Rev.* **2002**, *102* (6), 1929–1952. https://doi.org/10.1021/cr010319h.

(21) Meng, C.-Y.; Chen, H.; Wang, P.; Chen, L. Syntheses, Structures, and Magnetic and Thermoelectric Properties of Double-Tunnel Tellurides: $A_xRE_2Cu_{6-x}Te_6$ (A= K–Cs; RE= La–Nd). *Chem. Mater.* **2011**, *23* (22), 4910–4919.

(22) Mizuguchi, Y.; Miura, A.; Nishida, A.; Miura, O.; Tadanaga, K.; Kumada, N.; Lee, C. H.; Magome, E.; Moriyoshi, C.; Kuroiwa, Y. Compositional and Temperature Evolution of Crystal Structure of New Thermoelectric Compound $LaOBiS_{2-x}Se_x$. *J. Appl. Phys.* **2016**, *119* (15), 155103.

(23) Ishtiyak, M.; Panigrahi, G.; Jana, S.; Prakash, J.; Mesbah, A.; Malliakas, C. D.; Lebègue, S.; Ibers, J. A. Modulated Linear Tellurium Chains in Ba_3ScTe_5: Synthesis, Crystal Structure,

Optical and Resistivity Studies, and Electronic Structure. *Inorg. Chem.* **2020**, *59* (4), 2434–2442.

(24) Panigrahi, G.; Berseneva, A. A.; Morrison, G.; King, A. A.; Conner, R. L.; Jacobsohn, L. G.; zur Loye, H.-C. Crystal Growth of Quaternary $AkRE_2Si_2S_8$ (Ak = Ca and Sr; RE = La–Tb) Thiosilicates Using Flux-Assisted Boron Chalcogen Mixture Method: Exploring X-Ray Scintillation, Luminescence, and Magnetic Properties. *Inorg. Chem.* **2024**, *63* (28), 12849–12857.

(25) Yadav, S.; Swati; Niranjan, M. K.; Prakash, J. Syntheses and Characterization of $Ba_{16}Si_8Te_{44+\delta}$ and $Ba_6Si_4Te_6(Te_3)_3$ Structures with Complex Te–Te Interactions. *Inorg. Chem.* **2025**, *64* (2), 941–952.

(26) APEX3 Version 2019.1-0 and SAINT+ Version 8.40A. Bruker Nano, Inc., Madison, WI, USA, 2019.

(27) SADABS-2016/2: Krause, L., Herbst-Irmer, R., Sheldrick G.M. and Stalke D. J. Appl. Cryst. 2015, 48, 3-10.

(28) (A) SHELXT: Sheldrick, G.M. Acta Cryst. 2015, A71, 3-8. (b) SHELXL: Sheldrick, G.M. Acta Cryst. 2015, C71, 3-8.

(29) ShelXle: A Qt Graphical User Interface for SHELXL. Hübschle, C. B., Sheldrick, G. M., Bittrich, B. J. Appl. Cryst. 2011,.

(30) Kresse, G.; Furthmüller, J. Efficiency of Ab-Initio Total Energy Calculations for Metals and Semiconductors Using a Plane-Wave Basis Set. *Comput. Mater. Sci.* **1996**, *6* (1), 15–50.

(31) Kresse, G.; Joubert, D. From Ultrasoft Pseudopotentials to the Projector Augmented-Wave Method. *Phys. Rev. B* **1999**, *59* (3), 1758–1775.

(32) Blöchl, P. E. Projector Augmented-Wave Method. *Phys. Rev. B* **1994**, *50* (24), 17953–17979.

(33) Perdew, J. P.; Burke, K.; Ernzerhof, M. Generalized Gradient Approximation Made Simple. *Phys. Rev. Lett.* **1996**, *77* (18), 3865–3868.

(34) Ong, S. P.; Richards, W. D.; Jain, A.; Hautier, G.; Kocher, M.; Cholia, S.; Gunter, D.; Chevrier, V. L.; Persson, K. A.; Ceder, G. Python Materials Genomics (Pymatgen): A Robust, Open-Source Python Library for Materials Analysis. *Comput. Mater. Sci.* **2013**, *68*, 314–319.

(35) Zunger, A.; Wei, S.-H.; Ferreira, L. G.; Bernard, J. E. Special Quasirandom Structures. *Phys. Rev. Lett.* **1990**, *65* (3), 353–356.

(36) van de Walle, A.; Tiwary, P.; de Jong, M.; Olmsted, D. L.; Asta, M.; Dick, A.; Shin, D.; Wang, Y.; Chen, L.-Q.; Liu, Z.-K. Efficient Stochastic Generation of Special Quasirandom Structures. *Calphad* **2013**, *42*, 13–18.

(37) Chen, Z.-R.; Xu, H.-P.; Yao, W.-D.; Li, M.-Y.; Zhao, C.-Y.; Liu, W.; Guo, S.-P. Introduction of Diverse Divalent Main-Group Metal Cations to Tune the Physical Properties of Rare-Earth Thiophosphates. *Inorg. Chem.* **2025**, *64* (30), 15353–15358.

(38) Kashem, H. B.; Panigrahi, G.; Morrison, G.; Gabilondo, E. A.; Halasyamani, P. S.; Wisesa, P.; Besmann, T. M.; zur Loye, H.-C. Crystal Growth of Quaternary Rare Earth Selenosilicates by Using the Flux-Assisted Boron Chalcogen Mixture Method: Investigation of Their Magnetic and Optical Properties. *Cryst. Growth Des.* **2025**, *25* (11), 3767–3775.

(39)Panigrahi, G.; Binte Kashem, H.; Morrison, G.; zur Loye, H.-C. Synthesis of a Series of Rare-Earth-Based Multi-Anion Chalcogenide Iodides $RE_3Si_2Se_xS_{8-x}I$ (RE = La, Ce, Pr, and Nd) Using the Flux-Assisted Boron–Chalcogen Mixture Method. *Dalton Trans.* **2025**, *54* (15), 6252–6260.

(40) Berseneva, A. A.; Klepov, V. V.; Pal, K.; Seeley, K.; Koury, D.; Schaeperkoetter, J.; Wright, J. T.; Misture, S. T.; Kanatzidis, M. G.; Wolverton, C.; Gelis, A. V.; zur Loye, H.-C. Transuranium Sulfide via the Boron Chalcogen Mixture Method and Reversible Water Uptake in the $NaCuTS_3$ Family. *J. Am. Chem. Soc.* **2022**, *144* (30), 13773–13786.

(41) Bera, T. K.; Iyer, R. G.; Malliakas, C. D.; Kanatzidis, M. G. Eu3(AsS4)2 and AxEu3-yAs5-zS10 (A = Li, Na): Compounds with Simple and Complex Thioarsenate Building Blocks. *Inorg. Chem.* **2007**, *46* (21), 8466–8468. https://doi.org/10.1021/ic701067r.

(42) Lee, S.-P.; Huang, C.-H.; Chan, T.-S.; Chen, T.-M. New Ce^{3+}-Activated Thiosilicate Phosphor for LED Lighting—Synthesis, Luminescence Studies, and Applications. *ACS Appl. Mater. Interfaces* **2014**, *6* (10), 7260–7267.

(43)Shi, Y.-F.; Chen, Y.; Chen, M.-C.; Wu, L.-M.; Lin, H.; Zhou, L.-J.; Chen, L. Strongest Second Harmonic Generation in the Polar R_3MTQ_7 Family: Atomic Distribution Induced Nonlinear Optical Cooperation. *Chem. Mater.* **2015**, *27* (5), 1876–1884.

(44)Kamm, F.; Pielnhofer, F.; Schlosser, M.; Pfitzner, A. Synthesis and Characterization of $Na_4Si_2Se_6$-tP24 and $Na_4Si_2Se_6$-oP48, Two Polymorphs with Different Anionic Structures. *Inorg. Chem.* **2023**, *62* (28), 11064–11072.

(45) Menezes, L. T.; Assoud, A.; Kleinke, H. Crystal Structure, Phase Width, and Physical Properties of the Barium Tetrel Selenides $Ba_6Si_{2-x}Ge_xSe_{12}$ (x = 0, 0.5, 1, and 1.5) with Ultralow Thermal Conductivity. *Dalton Trans.* **2023**, *52* (43), 15831–15838.

(46)Nian, L.; Wu, K.; He, G.; Yang, Z.; Pan, S. Effect of Element Substitution on Structural Transformation and Optical Performances in $I_2BaMIVQ_4$ (I = Li, Na, Cu, and Ag; MIV = Si, Ge, and Sn; Q = S and Se). *Inorg. Chem.* **2018**, *57* (6), 3434–3442.

(47)Klepov, V. V.; Breton, L. S.; Pace, K. A.; Kocevski, V.; Besmann, T. M.; zur Loye, H.-C. Size-Driven Stability of Lanthanide Thiophosphates Grown from an Iodide Flux. *Inorg. Chem.* **2019**, *58* (9), 6565–6573.

(48)Daszkiewicz, M.; Gulay, L. D.; Lychmanyuk, O. S.; Pietraszko, A. Crystal Structure of the $R_3Ag_{1-\delta}SiS_7$ (R= La, Ce, Pr, Nd, Sm, δ = 0.10–0.23) Compounds. *J. Alloys Compd.* **2008**, *460* (1–2), 201–205.

(49) Mishra, V.; Mumbaraddi, D.; Iyer, A. K.; Mar, A. Rare-Earth Indium Selenides RE_3InSe_6 (*RE* = La−Nd, Sm, Gd, Tb): Structural Evolution from Tetrahedral to Octahedral Sites. *J. Solid State Chem.* **2021**, *297*, 122096.

(50) Yin, W.; Zhang, D.; Zhou, M.; Iyer, A. K.; Pöhls, J.-H.; Yao, J.; Mar, A. Quaternary Rare-Earth Selenides $Ba_2REGaSe_5$ and $Ba_2REInSe_5$. *J. Solid State Chem.* **2018**, *265*, 167–175.

(51) Yin, W.; K. Iyer, A.; Lin, X.; Li, C.; Yao, J.; Mar, A. Quaternary Chalcogenides $BaRE_2In_2Ch_7$ (RE = La – Nd; Ch = S, Se) Containing $InCh_5$ Trigonal Bipyramids. *Dalton Trans.* **2016**, *45* (31), 12329–12337.

(52) Guo, S.-P.; Chi, Y.; Guo, G.-C. Syntheses, Crystal Structures and Magnetic Properties of Ternary Rare-Earth Zirconium Selenides, Ln_2ZrSe_5 (Ln = Ce–Nd). *J. Alloys Compd.* **2016**, *676*, 101–105.

(53) Gao, L.; Xu, J.; Tian, X.; Zhang, B.; Wu, X.; Wu, K. $AgGaSe_2$-Inspired Nonlinear Optical Materials: Tetrel Selenides of Alkali Metals and Mercury. *Chem. Mater.* **2022**, *34* (13), 5991–5998.

(54) He, J.; Wang, Z.; Zhang, X.; Cheng, Y.; Gong, Y.; Lai, X.; Zheng, C.; Lin, J.; Huang, F. Synthesis, Structure, Magnetic and Photoelectric Properties of $Ln_3M_{0.5}M'Se_7$ (Ln = La, Ce, Sm; M = Fe, Mn; M′ = Si, Ge) and $La_3MnGaSe_7$. *RSC Adv.* **2015**, *5* (65), 52629–52635.

For Table of Content Use Only:

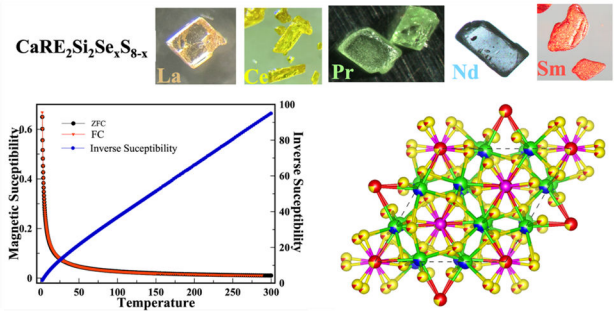

We report the synthesis and structural characterization of ten quaternary seleno-thiosilicates and selenosilicates, $AkRE_2Si_2Se_xS_{8-x}$and $CaRE_2Si_2Se_8$ (Ak = Ca, Sr; RE = La, Ce, Pr, Nd, Sm), prepared using the flux-assisted boron chalcogen mixture (BCM) method. Polycrystalline powders were used for magnetic and optical measurements. $CaCe_2Si_2Se_{1.73}S_{6.27}$ and $CaNd_2Si_2Se_{2.5}S_{5.5}$ show paramagnetic behavior, while UV–vis diffuse reflectance data revealed tunable band gaps from 2.0 to 2.7 eV. Photoluminescence was observed in $CaCe_2Si_2Se_{1.73}S_{6.27}$ under 375 nm UV excitation.